Three-Dimensional Imaging of a Single Dopant in a Crystal

Ryo Ishikawa,[1,2,*] Naoya Shibata,[1,3] Takashi Taniguchi,[4] and Yuichi Ikuhara[1,3]

[1] *Institute of Engineering Innovation, University of Tokyo, Bunkyo, Tokyo, 113-8656, Japan*
[2] *Japan Science and Technology Agency, PRESTO, Kawaguchi, Saitama 332-0012, Japan*
[3] *Nanostructures Research Laboratory, Japan Fine Ceramics Center, Nagoya, Aichi 456-8587, Japan*
[4] *Advanced Key Technologies Division, National Institute for Materials Science, Tsukuba 305-0044, Japan*

(Received 24 June 2019; revised manuscript received 10 February 2020; accepted 6 March 2020; published 26 March 2020)

Single dopants in materials have strong influences on the fundamental properties in extensive fields. Annular dark-field scanning tranmission electron microscopy (ADF STEM) has been contributed to directly investigate the occupation site of single dopants and their spatial distributions at atomic scale. However, the resultant atomic resolution images are projected in two dimensions, lacking in depth information. Here, we demonstrate the direct determination of three-dimensional atomic locations of single Ce dopants embedded in cubic boron nitride by ADF STEM depth sectioning with a significantly large illumination angle of 63 mrad in semiangle. Furthermore, we directly evaluate the Ce-Ce partial pair distribution function in the considerably long distance up to 8.5 nm, which opens the way to study a far-long-range interaction between impurities especially in a dilute doping system.

DOI: 10.1103/PhysRevApplied.13.034064

I. INTRODUCTION

Imperfection in semiconducting or insulating solids such as vacancies or impurities are the key to control their fundamental properties. To discover a new functionality in solids, impurity doping has long been used as an effective strategy in many fields [1]. One example is optoelectronic materials, where dopants act as luminescent centers and we can tailor pure transparent materials into light-emitter sources [2]. In addition to the occupation site of the dopants, the luminescent quantum efficiency is considered to be strongly affected by the interatomic distance between dopants: the emitted light may be nonradiatively absorbed by the other luminescent centers in case the distance between dopants is too short, as in several nanometers [3]. This phenomenon is known as concentration quenching that is especially active at high-doping levels, and it is therefore important to reveal the spatial distribution of dopants at atomistic scale. Annular dark-field scanning tranmission electron microscopy (ADF STEM) has a great capability to directly visualize single dopants not only on the surface but also embedded in solids [4–9]. However, the recorded ADF STEM images of single dopants are projected in two dimensions (2D), and it is thus difficult to measure the interatomic distances between dopants in true three dimensions (3D) from the images. Even with the recent advanced 3D electron microscopy such as electron tomography [10,11], it is still a major challenge to directly identify the 3D locations of point defects at atomic level, particularly with standard wedge-shape TEM samples rather than nanoparticles or needle-shape samples [12]. It is therefore essential to develop another approach to directly investigate the 3D location of individual single dopants inside materials.

Following the establishment of aberration-correction optics for electron microscopy, a wide variety of atomic scale problems in physics, chemistry, and materials science have been solved [13]. The spatial resolution in STEM has recently achieved 40.5 pm—less than half an angstrom—and this resolution is much greater than interatomic spacings in crystals [14]. However, such high spatial resolution is only obtained for lateral in two dimensions and the depth resolution along the axial direction is still no better than 5–10 nm in STEM. Since the depth resolution in STEM is physically limited by the illumination angle (α), there is still plenty of room to improve the depth resolution by the recent advanced electron optics [15]. Once an electron probe with a higher depth resolution is realized, we can acquire a focal series of atomic resolution images and construct 3D structure, so called depth sectioning [16]. Recently, we have equipped a DELTA-type aberration corrector [17] in JEM-ARM300CF electron microscope installed at the University of Tokyo, and the flat region in Ronchigram is stunningly enhanced up to 70 mrad in semiangle [14]. This value is almost two times larger than the previous generation of ETA-type corrector (α is less than 32 mrad) [18]. In this study, we demonstrate substantial improvement of the depth

*ishikawa@sigma.t.u-tokyo.ac.jp

resolution in atomic resolution ADF STEM by increasing the illumination angles. With the largest illumination angle of 63 mrad at 300 kV, we achieve the depth resolution of 2.14 nm. The depth sectioning with the aid of profile fitting allows us to directly determine the 3D locations of single Ce dopants embedded in a cubic boron nitride (c-BN) crystal [9] without any systematic image simulations [19–21]. Unlike coherent diffraction experiments, we can directly evaluate the Ce-Ce partial pair distribution function (PDF) from the 3D real-space images exploiting the incoherent nature of ADF STEM images [22]. In this paper, we demonstrate sub-angstrom lateral resolution even with the larger illumination angles. Secondary, we show the illumination angle dependence of depth resolution by using ADF STEM depth sectioning. Finally, we demonstrate the direct determination of 3D distribution of single Ce dopants in c-BN by utilizing the largest illumination angle of 63 mrad. We further discuss how the local configurations of single Ce dopants may affect the quantum efficiency of the light emission even in a dilute doping system from the viewpoint of Ce-Ce partial PDF.

II. EXPERIMENTAL AND SIMULATION METHODS

The Ce-doped c-BN is prepared by high-pressure and high-temperature conditions (5 GPa, 1773 K), and the details can be found in Ref. [9]. The electron transparent thin TEM specimen is prepared by a mechanical polishing and subsequent Ar-ion beam milling. To eliminate hydrocarbon contamination, the TEM sample and the specimen holder are baked at 353 K for a day in a clean vacuum and then transferred into the microscope. Atomic resolution ADF STEM images are acquired with an ARM300CF installed at the University of Tokyo, equipped with a JEOL DELTA corrector, cold-field emission gun operated at 300 kV. To select illumination angles, we use six different-sized apertures with a fixed condenser lens condition. To stably set the same beam current in different α, we change the extraction voltage of the electron gun in the range from 3.0 to 3.4 kV rather than changing in condenser lens or gun lens, where one can precisely control the beam current with maintaining the same optical condition such as geometric aberrations. We also note that the present beam current is relatively small and therefore the improvement of the energy spread via smaller extraction voltage could be negligibly small. To stably and precisely operate the probe position along the depth, we adopted a high-tension focus system (δE) rather than a conventional objective-lens focus system, where the high tension is electrostatically controllable and we are free from magnetic hysteresis and incidental thermal instability for the objective lens. The C_c is accurately measured to be 1.75 ± 0.01 mm by using systematic coherent convergent-beam-electron diffraction-pattern analysis [23]. The minimum energy step of δE is 10 meV corresponding to a depth of 0.58 Å via $\delta z = C_c\,(\delta E\,/E_0)$, and this precision is enough to scan the probe along the depth. To include chromatic aberration effects in image simulation, we experimentally measure the zero-loss profile by using electron energy-loss spectroscopy (Quantum ER, Gatan Inc.) and the energy spread is 0.34 eV in full width at half maximum.

The image simulations are performed using the frozen phonon model with a 300-kV probe and illumination semiangles of 30, 40, 50, and 63 mrad. The Debye-Waller (DW) factors for B and N in c-BN are referred to in previous report [24]. Since there is no report for the DW factor of the single Ce dopants in c-BN, we use the inverse mass-scaled DW factor for the single Ce dopant from N atom in c-BN. It is noteworthy that we also test in several different DW factors for the single Ce dopants, the difference is negligibly small. The supercell structure model is used for the image simulations, where the specimen thickness is 13.9 nm (54 atoms in projection) and a single Ce dopant is located in the middle of the sample (27th depth from the entrance). The 30 focal series of ADF STEM images with 4.6 Å focus step are calculated for respective illumination angles. To include the finite-source-size effect, the calculated images are convolved with a Gaussian source size of 0.64 Å in full width at half maximum. To further include chromatic aberration effect in simulations, these focal series images are convolved with the defocus spread function based on our previous report [25].

III. RESULTS AND DISCUSSION

A. Lateral resolution

Correcting geometric aberrations up to sixth-fold astigmatism ($<60\ \mu$m) by the DELTA corrector, the flat region in a Ronchigram has extended up to 70 mrad. However, the effect of chromatic aberration becomes severe as increasing α, and the lateral ($r_\perp$) spatial resolution would become worse in a larger α: $d_{r_\perp} = \sqrt{(0.61\lambda/\alpha)^2 + (C_c\Delta E\alpha/E_0)^2}$, where λ is electron wavelength, C_c is a chromatic aberration coefficient, ΔE is an energy spread, and E_0 is an incident electron energy of the electron source. Our lateral resolution is maximized around 40 mrad and then decreases with the larger α due to the chromatic aberration [14,23]. In the depth resolution, on the other hand, the effect of chromatic aberration has no dependence on α, and the depth resolution will be simply improved as a function of α [25]:

$$d_z = \sqrt{(d_0\lambda/\alpha^2)^2 + (C_c\Delta E/E_0)^2}, \qquad (1)$$

where d_0 is a constant and usually used in the range of $1 \leq d_0 \leq 2$ [26]. The larger α is therefore suitable to perform depth sectioning. Since STEM imaging with the larger α becomes crucially sensitive to the tiny amount of residual geometric aberrations, care is needed for simultaneously keeping both high lateral and depth resolution with the larger α.

To investigate an illumination angle dependence for the lateral resolution, we acquire ADF STEM images of *c*-BN viewed along the [110] direction by using 9, 20, 30, 40, 50, and 63 mrad, respectively, as shown in Fig. 1. These images are recorded at the same area and with the same beam current of 11.4 ± 0.2 pA, and the specimen thickness is roughly estimated to be 8 nm via the log-ratio method in electron energy-loss spectroscopy [27]. The interspacing of B-N dumbbell in the projection is 0.9 Å, and the dumbbell recorded with 9 mrad of Fig. 1(a) is not resolved because of its diffraction limit. With the illumination angles larger than 20 mrad, the B-N dumbbell is well resolved in Figs. 1(b)–1(f), guaranteeing that sub-angstrom lateral resolution is achievable even with 63 mrad, although Figs. 1(e) and 1(f) are slightly suffered by residual geometric aberrations. When a probe spread along the depth becomes smaller, the ADF intensity at an

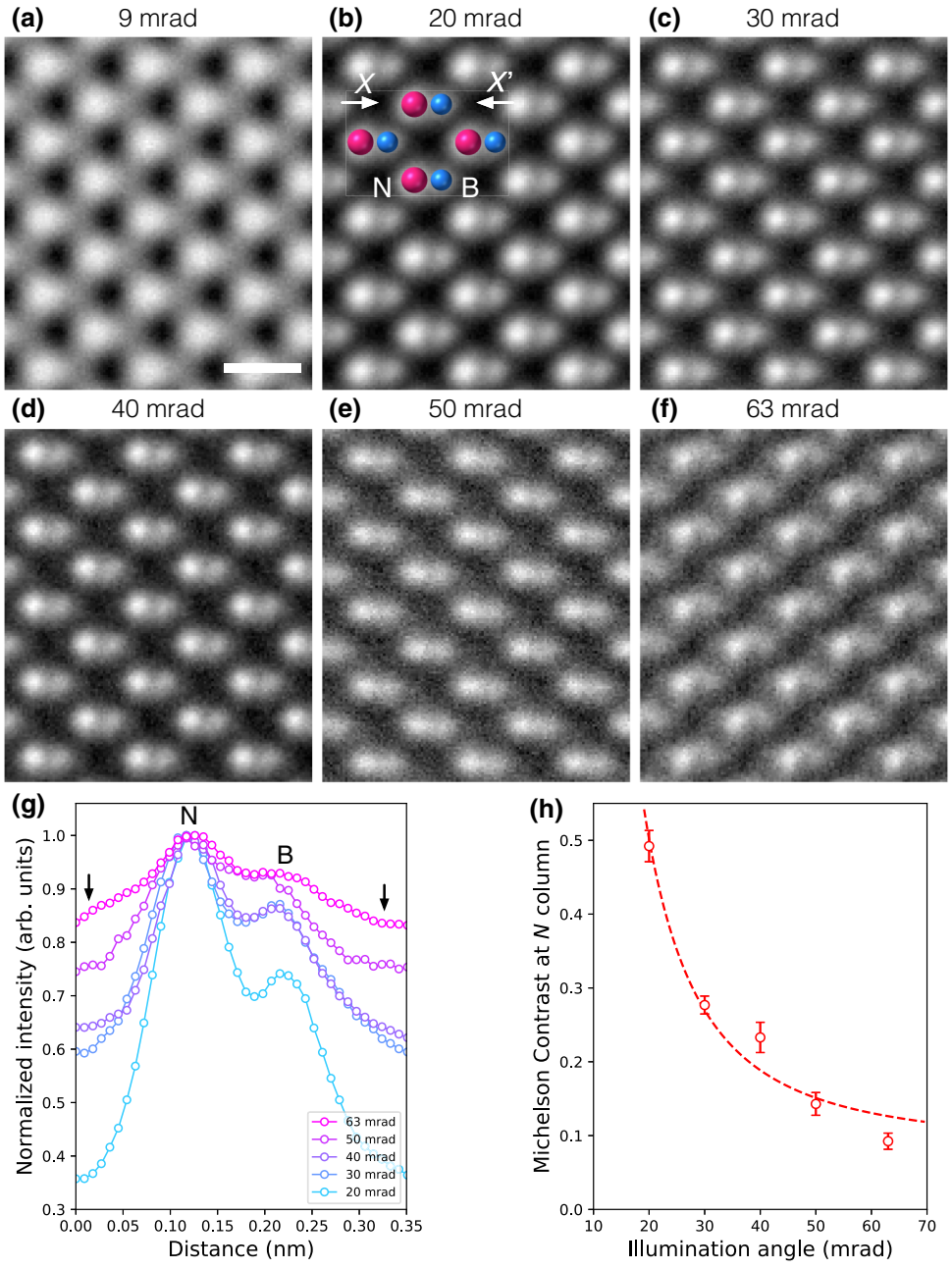

FIG. 1. Atomic resolution ADF-STEM images of *c*-BN viewed along the [110] direction with the illumination semiangles of (a) 9, (b) 20, (c) 30, (d) 40, (e) 50, and (f) 63 mrad, respectively. (g) Normalized ADF intensity profiles along X-X′ direction in (b) with various illumination angles. (h) Michelson contrast at N column as a function of illumination angle, where the error bars are the standard error of the mean (±3 SEM). The scale bar in (a) is 2 Å.

atomic column will be reduced because the total number of atoms along the depth contributing to the ADF intensity becomes smaller. In other words, the background level at an interstitial site will be increased relative to that at the atomic column, and therefore the ADF contrast at the atomic column will be reduced as a function of α. This effect can be seen in the normalized intensity profiles along X-X′ direction in Fig. 1(g), where the background levels at arrows increase as a function of α. To evaluate the visibility of the atomic column in ADF STEM, we use Michelson contrast (C_M):

$$C_M = \frac{I_{\max} - I_{\min}}{I_{\max} + I_{\min}}, \tag{2}$$

where $I_{\max}$ and $I_{\min}$ are the maximum intensity at the column and the background level as indicated by arrows in Fig. 1(g). Figure 1(h) shows Michelson contrast at nitrogen column as a function of α, and it is clearly shown the contrast reduction with the dependence of α^{-2} (fitted dashed line), which is expected from Eq. (1). Although Michelson contrast is a simple indicator to evaluate the atomic column visibility, the observed reduction of Michelson contrast as a function of α suggests that the total number of atoms along the depth could be reduced as a function of α^{-2}. This result strongly supports the improvement of the depth sensitivity by the larger α, and the largest illumination angle of 63 mrad may be appropriate for depth sectioning.

B. Depth resolution

To investigate the relationship between depth sensitivity and the illumination angle, we acquire a focal series of ADF STEM images obtained from *c*-BN:Ce viewed along the [110] direction (60–100 frames, 512 × 512 pixels, focus step is 4.6 Å). The experiments with different illumination angles are carried out in similar thicknesses of 14 to 18 nm. Figure 2(a) shows the tabulated focal series of experimental ADF STEM images of primitive cells containing a single Ce dopant with 30, 40, 50, and 63 mrad, where the Ce atoms are substituted for nitrogen site [9]. To statistically analyze the 3D data sets, we evaluate the focal images by the values of "mean" and "standard deviation" within a white-circular-area shown on the top left of Fig. 2(b). Since the interspace between B and N atomic columns is considerably close as 0.9 Å in projection, the size of the white-circular-area becomes relatively small. However, the white-circular-area contains 208 pixels and it still has statistically meaningful information, even for the noise sensitive "standard deviation" analysis. Figure 2(c) shows the mean depth profiles at the single Ce-containing atomic columns, where the values are normalized by the maximum value for respective depth profiles. To determine the Ce-depth location (peak position), we perform Gaussian fitting for respective mean depth profiles:

$$I(z) = a \exp\left(-\frac{(z - z_p)^2}{2\sigma_z^2}\right) + b, \tag{3}$$

where the fitting parameters of a, b, z_p, σ_z are amplitude, background, peak position, and standard deviation, respectively. The fitted Gaussian profiles (solid lines) are overlaid on the mean depth profiles of Fig. 2(c). We note that, in a first approximation, a focal series of ADF STEM images may be described well as the convolution of Gaussian kernels with an optimum focused image, and it is therefore reasonable to adopt the Gaussian profile for the fitting of the depth profiles. With 30 mrad, the experimental mean values within the dashed box in Fig. 2(c) show strong deviations from the fitted curve, and in fact the degree of Gaussian fit is the lowest. It is therefore less reliable to determine the Ce-depth location with 30 mrad. While in the larger α, the degree of curve fitting is more accurate and the peak positions of the fitted Gaussian profiles are well matched with the respective maximum mean values, suggesting that the larger α has higher reliability to determine the depth locations of Ce dopants. From the statistical viewpoint, the depth resolution can be defined as the standard deviation of the fitted Gaussian profile [$2\sigma_z$ in Eq. (3)], corresponding to the width of the 68% confidence intervals of the fitted curve, and we hereafter denote as ${\sigma_z}^{\text{mean}}$ [$=2\sigma_z$, given in Fig. 2(c)]. However, the estimated depth resolution from the mean depth profiles of ${\sigma_z}^{\text{mean}}$ are 6.2 and 5.1 nm for 40 and 63 mrad, respectively. These values are much poorer depth resolutions than those expected from Eq. (1). While in the "standard deviation" depth profile of Fig. 2(d), it exhibits much narrower profiles than those in the mean depth profiles of Fig. 2(c). In a similar manner of the mean-depth-profile analysis, we perform Gaussian fitting for the "standard deviation" depth profiles by using Eq. (3) and the fitted Gaussian profiles (solid lines) are overlaid on Fig. 2(d). Unlike the mean depth profiles, the ${\sigma_z}^{\text{std}}$ [$=2\sigma_z$ in Eq. (3)] of the "standard deviation" depth profile becomes remarkably narrower down with the larger α, and the ${\sigma_z}^{\text{std}}$ is reasonably high-depth sensitivity as expected from Eq. (1). As we mention, the defocused ADF STEM image may be approximately described by the convolution of a Gaussian kernel with an optimum focused image. In a Gaussian convolved image, the intensity redistribution occurs, but the mean value will be ideally unchanged even in a subarea (or white-circular-area), suggesting that the mean depth profile is insensitive as a function of defocus. Although the mean value is unchanged by the Gaussian convolution, the respective pixel intensities at the Ce-containing atomic column becomes closer to each other. It is therefore the standard deviation within the white-circular-area quickly

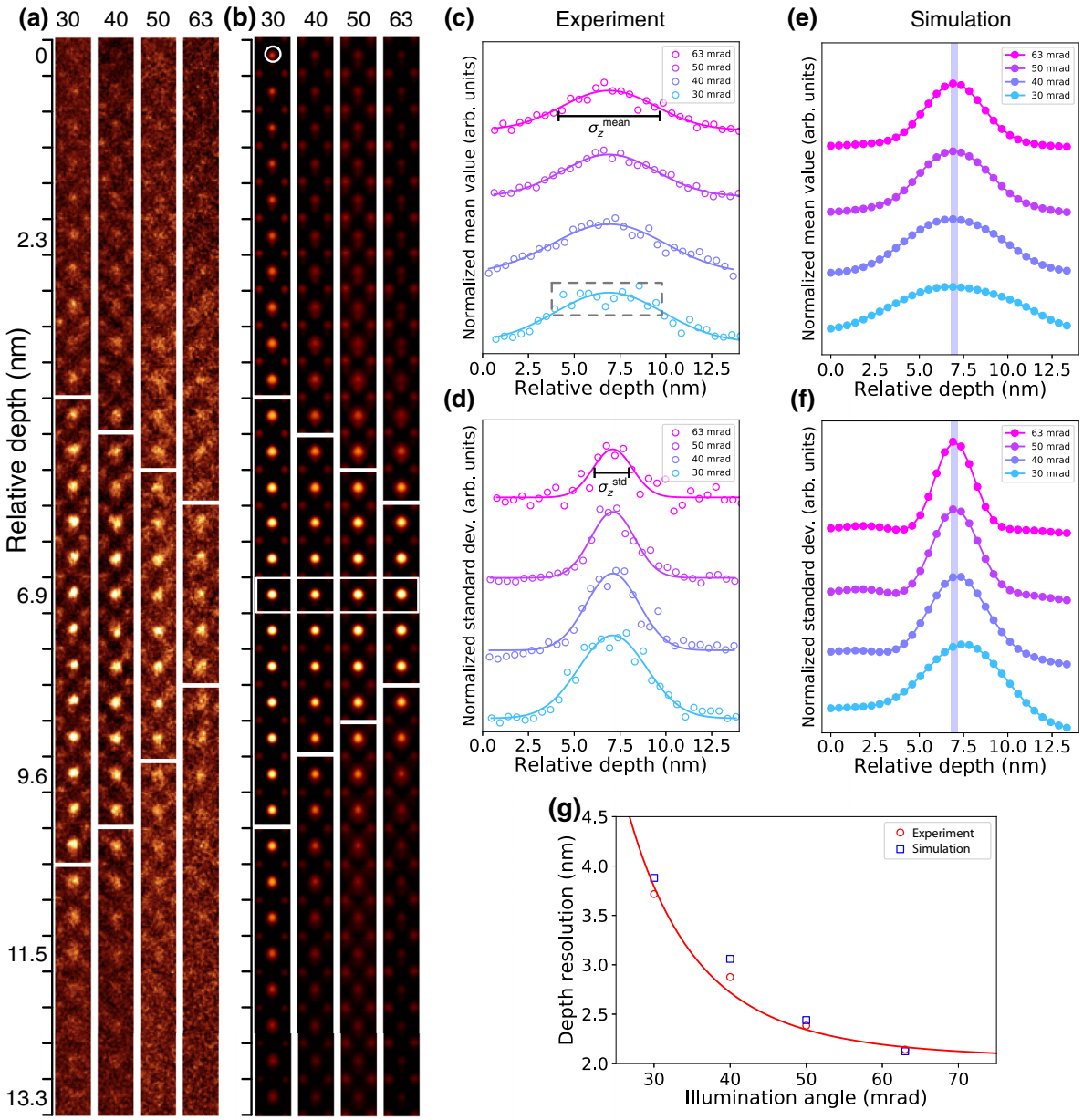

FIG. 2. (a) Focal series of experimental ADF STEM images obtained from *c*-BN viewed along the [110] direction with respective illumination angles of 30, 40, 50, and 63 mrad, where the Ce-containing primitive cell is tabulated along the depth with 4.6 Å step. (b) The simulated focal series ADF STEM images in the same manner as (a), where the specimen thickness is 13.9 nm (54 atoms in projection) and the single Ce dopant is located at 27th from the entrance surface, as indicated by the white box. (c) The experimental mean and (d) the standard deviation depth profiles and the fitted Gaussian profiles (overlaid solid lines) obtained from the Ce-containing column as a function of relative depth with respective to the illumination angles. (e) The simulated mean and (f) the standard deviation depth profiles of (b). The transparent blue rectangles in (e), (f) indicate the depth location of the single Ce dopant in the model. (g) The experimentally measured depth resolution (σ_z^{std}) as a function of illumination angle and the fitted curve ($d_0 = 1.46$) by using Eq. (1).

reduces as a function of defocus, suggesting that the "standard deviation" depth profile is suitable to measure the depth resolution.

To confirm the validity of our experimental depth sectioning, we perform focal-series ADF STEM image simulations for respective α, where the specimen thickness of the model structure has 13.9 nm (54 atoms in projection) and a single Ce dopant at the nitrogen site [9] is located in 27th depth from the entrance surface. To directly compare the simulations with the experimental

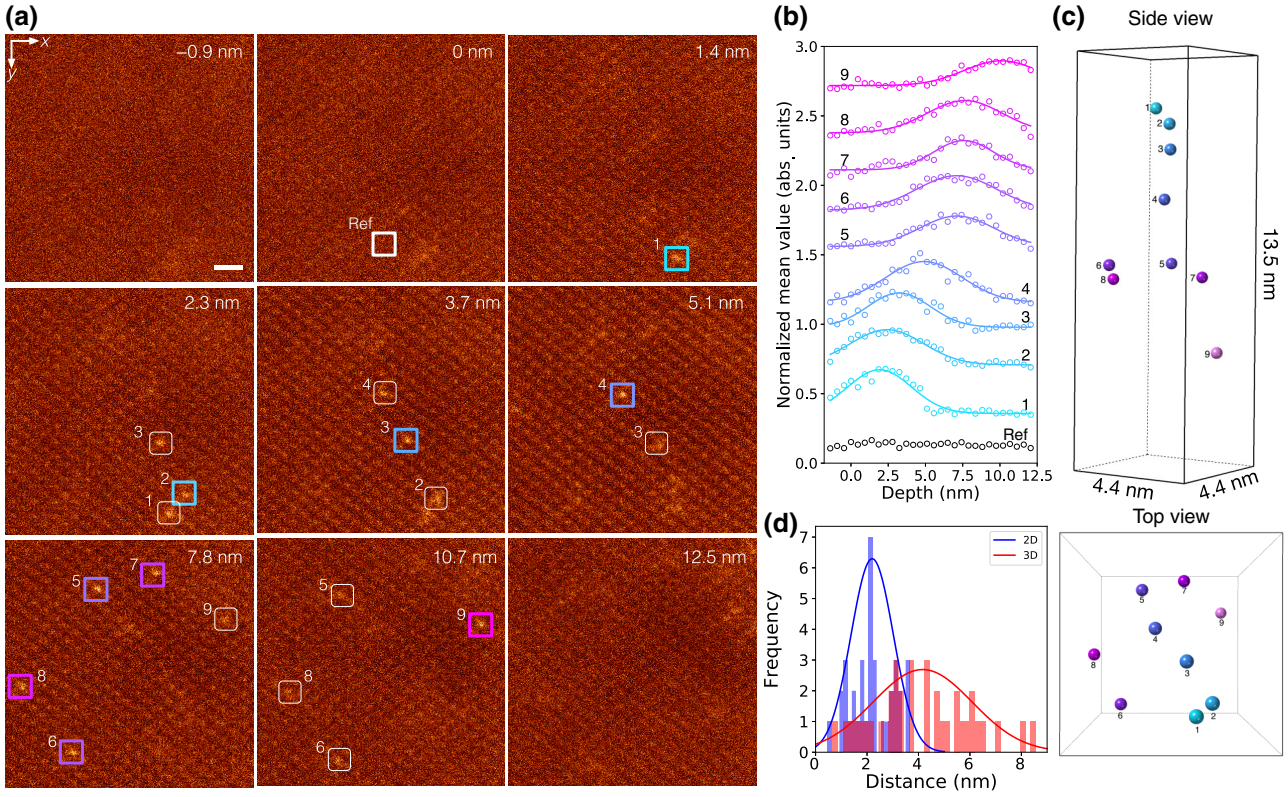

FIG. 3. (a) Selected frames from a focal series of ADF STEM images obtained from *c*-BN:Ce viewed along the [110] orientation, where the illumination angle is 63 mrad and the depth for each panel is given in the right top. The locations of the single Ce dopants are labelled with serial numbers and marked by colored squares. The white rounded squares indicate the residual weak contrasts from the corresponding single Ce dopants. (b) The mean depth profiles and the fitted Gaussian profiles for each single Ce dopants and the corresponding serial numbers are given in the same manner as (a). (c) Spatial distribution of single Ce dopants in 3D from top and side views, respectively. (d) The directly calculated the Ce-Ce partial PDF based on Table I in the respective forms of projected 2D and 3D, where solid lines are the fitted Gaussian profiles. The scale bar in (a) is 5 Å.

data, we include effective source size and chromatic aberration effects in the simulated images with the measured C_c and ΔE of our microscope, based on our previous report [25]. Figure 2(b) shows the tabulated focal series of the simulated ADF STEM images in the same manner of the experiment in Fig. 2(a). As increasing α, the brighter Z-contrast contributions from the single Ce dopant are more localized along the depth, which is excellently matched with the experimental images. To statistically evaluate the simulated images, we further investigate the depth profiles in the views of mean value and standard deviation at the Ce-containing atomic column, as shown in Figs. 2(e) and 2(f), respectively. Although the simulated mean depth profiles show slightly better depth sensitivity than the experiments, the simulated depth profiles are well matched with the experiments, i.e., the simulated σ_z^{mean} for respective α are much larger than the depth resolution expected from Eq. (1). While in the simulated standard depth profiles, the σ_z^{std} is significantly improved as a function of α, which is also remarkably matched with the experiments of Fig. 2(d). It is noteworthy that the peak positions in the simulated "standard deviation" depth profiles with 30 and 40 mrad show slight shift toward deeper depth of ∼5 Å (2 unit cells) from the exact depth location of the single Ce dopant, suggesting that we cannot ignore the channeling effect even with the light nitrogen atomic column [28]. However, with α of 50 and 63 mrad, the peak positions of the simulated depth profiles are exactly matched with the single Ce dopant location. To further confirm the detection capability of the dopant depth, we perform focal series of ADF STEM image simulations, where the single Ce dopants are located at near the entrance surface (7th) and exit surface (38th), respectively (see Appendix). At closer the entrance surface (7th), it is possible to determine the dopant-depth location even with the smaller 30 mrad. While at the deeper-depth location (38th), the distinct peak position shift can be found in the "standard deviation" depth profiles with 30 or 40 mrad. However, with the

larger α than 50 mrad, the peak positions in the depth profiles are exactly matched with the true dopant positions in the model. Although we cannot completely remove the channeling effect, the probe channeling could be relatively suppressed with the larger α than 50 mrad, which is significantly powerful to determine the depth locations of single dopants.

Figure 2(g) shows the experimental σ_z^{std} as a function of α, and we achieve the highest depth resolution of $d_z = 2.14$ nm with 63 mrad, which is well compatible with the simulated σ_z^{std}. Although there are residual geometric aberrations with the larger α shown in Figs. 1(e) and 1(f), the measured depth resolution is not significantly affected by the present small amount of residual aberrations (undetectably small amount in the smaller α). This is because the present depth resolution is 20 times lower than the lateral resolution. Since we know C_c and ΔE in our microscope, the parameter d_0 is now estimated to be 1.46 by fitting the experimental data of Fig. 2(d) in accordance with Eq. (1). Even with the illumination angle of 63 mrad, we cannot completely remove dynamical effects, and it is therefore reasonable to use 1.46 rather than 1.0 for the parameter d_0, although the parameter d_0 can be improved by removing the residual geometric aberrations. Under the condition, the depth resolution is estimated to be 2.0 nm even with the illumination angle of 100 mrad, because the depth resolution at such a larger α is mainly limited by chromatic aberration. For further improvement of depth resolution, it becomes essential to develop a new electron gun with extremely small energy spread less than 0.1 eV or a chromatic aberration corrector, nevertheless recent monochromated electron sources should be useful [29,30].

C. Three-dimensional distribution of single dopants

Utilizing the high-depth resolution of 63 mrad, we investigate 3D distribution of single Ce dopants in *c*-BN. A focal series of ADF STEM images are acquired with the focus step of 4.6 Å. Using a cross-correlation method, the total in-plane specimen drift for whole frames is estimated to be within the limits of 2.2 Å (drift rate is 7.6 pm/frame in average), and the specimen drift along the depth can be in the similar range. This drift rate is negligibly small, and we ignore the specimen drift along the depth in the following 3D analysis. Figure 3(a) shows the frames selected from the 3D data and the depth is given on the right top in each panel. At the first frame of Fig. 3(a), the probe is focused slightly above the entrance surface of the sample, and no atoms are visible. In the second panel of Fig. 3(a), the probe is just focused on the entrance surface and the *c*-BN lattice contrasts start to be formed, and we then assign this depth as an origin of z coordinate. At adepth of 2–3 nm, two single Ce dopants become visible as marked by the colored squares of no. 1, no. 2, although these contrasts are very weak at the first frame (weak contrasts of the Ce dopants are marked by white rounded squares in Fig. 3(a). At a depth of 4–5 nm, the other single Ce dopants of no. 3, no. 4 become brighter, while the intensities from no. 1, no. 2 rapidly decrease. At a frame of $z = 7.8$ nm, four more single Ce dopants of no. 5–no. 8 can be seen as bright dot contrasts. The last single Ce dopant of no. 9 is visualized even at the very deep depth of 10.7 nm. In the last panel of Fig. 3(a), the contrasts from all of the single Ce dopants are well suppressed, and moreover the *c*-BN lattice contrasts are almost vanishing because the probe is focused slightly above the exit surface of the sample. Using the lattice contrast of *c*-BN in the focal series of ADF STEM images, we determine the depth locations of entrance and exit surfaces, and the specimen thickness at this region is estimated to be 13.5 nm (52 atoms in projection), suggesting that the volume consists of 42 000 atoms ($4.4 \times 4.4 \times 13.5$ nm^3). To precisely determine the 3D locations of all the single Ce dopants, we perform Gaussian fitting (solid lines) for the mean depth profiles of Fig. 3(b). The resultant 3D locations of the nine single Ce dopants are visualized in Fig. 3(c) and summarized in Table I, where the nitrogen site on the left top of the frame in Fig. 3(a) is assigned to be an origin of xy coordinate. Since we know the interatomic distance between nitrogen atoms along the [110] direction, the depth locations of single Ce dopants can be described in a form of integer counted from the entrance surface, as shown in the right column of Table. I. Since the present depth resolution is 2 nm at most, it may be difficult to directly count the number of Ce dopants along the same atomic column. However, as our previous theoretical simulations, the mean depth profile becomes much broader when there are more than two Ce dopants in the same column, which is not the case in the present data. Therefore, we conclude that the present brighter atomic columns contain only one Ce dopant, respectively.

TABLE I. Three-dimensional locations of single Ce dopants in *c*-BN crystal, where the serial numbers correspond to the numbers in Fig. 2.

Ce	x (nm)	y (nm)	z (nm)	z
1	2.73	3.73	1.92	7
2	3.09	3.47	2.42	9
3	2.55	2.57	3.23	13
4	1.82	1.80	4.90	19
5	1.46	0.77	7.11	28
6	0.91	3.73	7.09	28
7	2.55	0.51	7.56	29
8	0.18	2.45	7.63	30
9	3.64	1.29	10.08	39

On a basis of 3D distribution of single Ce dopants, we here discuss the luminescent property of *c*-BN:Ce in the observed volume of Fig. 3(c). The Ce-doping level of the

present specimen is relatively low as $(2.6 \pm 0.1) \times 10^{18}$ atoms cm^{-3} [9], which corresponds to 9-nm interatomic distance between Ce atoms on average. Since the critical distance is typically in the range of 2–4 nm for inorganic materials with rare-earth single dopants [3], the concentration quenching may not be the case in the present system. However, at atomic scale, the local Ce concentration can be fluctuated, and in fact, the observed volume has ten times higher Ce concentration (approximately 3.4×10^{19} atoms cm^{-3}) than that on average, which suggests the possibility of local concentration quenching. To discuss the local concentration quenching in this volume, we investigate the distribution of Ce-Ce interatomic distances. Figure 3(d) shows the Ce-Ce partial PDF in 2D projection and 3D, respectively, where we directly calculate the Ce-Ce interatomic distances for 36 Ce-Ce pairs from Table I. In the 2D projection, the Ce-Ce partial PDF has a peak at 2.2 ± 0.82 nm, while in true three dimensions, the Ce-Ce pair PDF has a peak at 4.16 ± 1.93 nm, which is almost two times longer than that in 2D projection. It is therefore evidently shown as to how the interatomic distance is likely to be underestimated in 2D projection, and this underestimation will be problematic in thicker samples. Owing to the small Ce-Ce interatomic distance of 4.2 nm on average, half of the Ce-Ce pairs in this volume may contribute to the local concentration quenching, leading to the reduction of quantum efficiency of the light emission even in this low doping level. The present volume is not the special case, but we often observe such dopant-concentrated volumes. Since the Ce dopants are in the form of negatively charged complex point defects [9], the interaction between Ce dopants should be long-range Coulomb repulsive force. However, we also have carbon impurities in the similar level of Ce dopants [31], which exists in the form of positively charged point defect [32]. It is therefore the positively charged carbon point defects may be bridging sites to form a long-range attractive force between negatively charged Ce dopants and may stabilize the local high Ce concentration as a weak clustering rather than a uniform distribution of Ce dopants. Finally, it is noteworthy to point out that a PDF is typically measured in the distance range less than 2–3 nm because it is obtained from coherent x-ray, neutron, or electron diffraction experiments. However, the present ADF STEM is the incoherent imaging that is able to directly obtain 3D information, which has great advantages to investigate the long-range interactions between dopants especially in a dilute doping system.

IV. CONCLUSION

We demonstrate the substantial improvement on the depth resolution by using large-angle illumination STEM. With the largest illumination angle of 63 mrad, the achieved depth resolution is 2.14 nm, where we can maintain sub-angstrom lateral resolution. The advanced electron optics allows us to directly investigate 3D distribution of single Ce dopants in *c*-BN crystal at atomic scale, with high reliability. Using the 3D locations of Ce dopants, we directly derive the long-range Ce-Ce partial PDF in the dilute-doping system. The present long-range correlation analysis of the functional dopants in 3D should be helpful to understand the fundamental properties in solids.

ACKNOWLEDGMENTS

A part of this work is supported by the Research and Development Initiative for Scientific Innovation of New Generation Batteries (RISING2) project of the New Energy and Industrial Technology Development Organization (NEDO), Japan, and Japan Society for the Promotion of Science (JSPS) KAKENHI Grants No. 17H06094 and No. 19H05788. The authors thank Dr S. Morishita (JEOL) for the optimization of electron optics in this microscope. R.I. acknowledges the support from JSPS KAKENHI Grant No. 18H01823 and JST PRESTO.

APPENDIX: FOCAL SERIES OF ADF STEM IMAGE SIMULATIONS

In main text, we only show the simulated focal series of ADF STEM images, where a single Ce dopant is located in the middle of the sample. To establish the interpretation of Fig. 3, we further perform focal series of image simulations with different depth locations of single Ce dopants. Figure 4 shows the tabulated focal series of ADF STEM images in the same manner of Fig. 2(b), and the single Ce dopants are located at (a) 7th (1.6 nm) and (b) 38th (9.9 nm) from the entrance surface, respectively, where the sample thickness is 13.9 nm (54 atoms in projection). In the same manner as Figs. 2(e) and 2(f), we perform mean and "standard deviation" depth-profile analysis for the simulated ADF STEM images of Figs. 4(a) and 4(b), which are given in Figs. 4(c)–4(f), respectively. When the single Ce dopant is located near the entrance surface, it is possible to determine the depth location of the single Ce dopant even with 30 mrad. While in the case of the deeper-depth location of the single Ce dopant (38th), the peak positions with 30 mrad are slightly shifted from the exact depth location in both the mean and the "standard deviation" depth profiles of Figs. 4(e) and 4(f). However, with larger α of 50 or 63 mrad, the peak positions are well matched with the true Ce depth locations. Therefore, we can directly determine the depth locations of single Ce dopants from the experimental data set of Fig. 3(a).

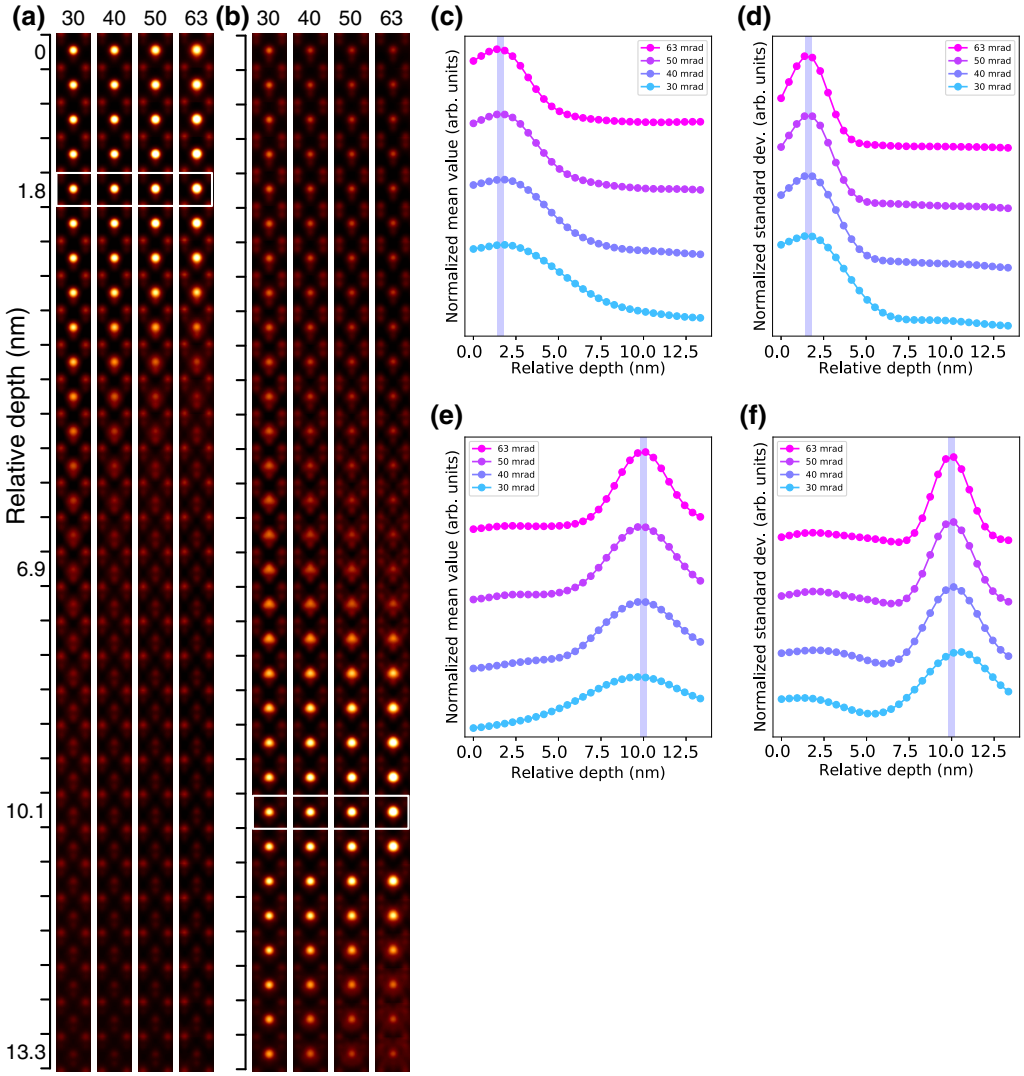

FIG. 4. The simulated focal series of ADF STEM image obtained from *c*-BN viewed along the [110] direction with respective illumination angles of 30, 40, 50, and 63 mrad, where the Ce-containing primitive cell is tabulated along the depth with 4.6 Å step. The single Ce dopants are located at (a) 7th ($z = 1.6$ nm), (b) 38th ($z = 9.9$ nm) from the entrance surface, as marked by white rectangles, respectively. The mean depth profiles for (a) and (b) are shown in (c) and (e), respectively. The "standard deviation" depth profiles for (a) and (b) are shown in (d) and (f), respectively. The transparent blue rectangles in (c)–(f) indicate the location of single Ce dopants.

[1] P. M. Koenraad and M. E. Flatte, Single dopants in semiconductors, Nat. Mater. **10**, 91 (2011).

[2] Leah Bergman and J. L. McHale, *Handbook of Luminescent Semiconductor Materials* (Taylor & Francis Group, New York, 2012).

[3] G. Blasse and B. C. Grabmaier, *Luminescent Materials* (Springer-Verlag, Berlin, 1994).

[4] A. V. Crewe, J. Wall, and J. Langmore, Visibility of single atoms, Science **168**, 1338 (1970).

[5] S. J. Pennycook and L. A. Boatner, Chemically sensitive structure-imaging with a scanning transmission electron microscope, Nature **336**, 565 (1988).

[6] P. M. Voyles, D. A. Muller, J. L. Grazul, P. H. Citrin, and H.-J. L. Gossmann, Atomic-scale imaging of individual dopant atoms and clusters in highly *n*-type bulk Si, Nature **416**, 826 (2002).

[7] P. D. Nellist and S. J. Pennycook, Direct imaging of the atomic configuration of ultradispersed catalysts, Science **274**, 413 (1996).

[8] N. Shibata, S. D. Findlay, S. Azuma, T. Mizoguchi, T. Yamamoto, and Y. Ikuhara, Atomic-scale imaging of individual dopant atoms in a buried interface, Nat. Mater. **8**, 654 (2009).

[9] R. Ishikawa, N. Shibata, F. Oba, T. Taniguchi, S. D. Findlay, I. Tanaka, and Y. Ikuhara, Functional Complex Point-Defect Structure in a Huge-Size-Mismatch System, Phys. Rev. Lett. **110**, 065504 (2013).

[10] S. Van Aert, K. J. Batenburg, M. D. Rossell, R. Erni, and G. Van Tendeloo, Three-dimensional atomic imaging of crystalline nanoparticles, Nature **470**, 374 (2011).

[11] Y. Yang, C.-C. Chen, M. C. Scott, C. Ophus, R. Xu, A. Pryor, L. Wu, F. Sun, W. Theis, J. Zhou, M. Eisenbach, P. R. C. Kent, R. F. Sabirianov, H. Zeng, P. Ercius, and J. Miao, Deciphering chemical order/disorder and material properties at the single-atom level, Nature **542**, 75 (2017).

[12] R. Xu, C.-C. Chen, L. Wu, M. C. Scott, W. Theis, C. Ophus, M. Bartels, Y. Yang, H. Ramezani-Dakhel, M. R. Sawaya, H. Heinz, L. D. Marks, P. Ercius, and J. Miao,

Three-dimensional coordinates of individual atoms in materials revealed by electron tomography, Nat. Mater. **14**, 1099 (2015).

[13] S. J. Pennycook and P. D. Nellist, *Scanning Transmission Electron Microscopy Imaging and Analysis* (Springer, New York, 2011).

[14] S. Morishita, R. Ishikawa, Y. Kohno, H. Sawada, N. Shibata, and Y. Ikuhara, Attainment of 40.5 pm spatial resolution using 300 kV scanning transmission electron microscope equipped with fifth-order aberration corrector, Microscopy **67**, 46 (2018).

[15] R. Ishikawa, A. R. Lupini, Y. Hinuma, and S. J. Pennycook, Large-angle illumination STEM: Toward three-dimensional atom-by-atom imaging, Ultramicroscopy **151**, 122 (2015).

[16] K. van Benthem, A. R. Lupini, M. Kim, H. S. Baik, S. Doh, J.-H. Lee, M. P. Oxley, S. D. Findlay, L. J. Allen, J. T. Luck, and S. J. Pennycook, Three-dimensional imaging of individual hafnium atoms inside a semiconductor device, Appl. Phys. Lett. **87**, 034104 (2005).

[17] H. Sawada, T. Sasaki, F. Hosokawa, S. Yuasa, M. Terao, M. Kawazoe, T. Nakamichi, T. Kaneyama, Y. Kondo, K. Kimoto, and K. Suenaga, Correction of higher order geometrical aberration by triple 3-fold astigmatism field, J. Electron Microsc. **58**, 341 (2009).

[18] H. Sawada, N. Shimura, F. Hosokawa, N. Shibata, and Y. Ikuhara, Resolving 45-pm-separated Si–Si atomic columns with an aberration-corrected STEM, Microscopy **64**, 213 (2015).

[19] J. Hwang, J. Y. Zhang, A. J. D'Alfonso, L. J. Allen, and S. Stemmer, Three-Dimensional Imaging of Individual Dopant Atoms in $SrTiO_3$, Phys. Rev. Lett. **111**, 266101 (2013).

[20] C. L. Jia, S. B. Mi, J. Barthel, D. W. Wang, R. E. Dunin-Borkowski, K. W. Urban, and A. Thust, Determination of the 3D shape of a nanoscale crystal with atomic resolution from a single image, Nat. Mater. **13**, 1044 (2014).

[21] R. Ishikawa, A. R. Lupini, S. D. Findlay, T. Taniguchi, and S. J. Pennycook, Three-Dimensional location of a single dopant with atomic precision by aberration-corrected scanning transmission electron microscopy, Nano Lett. **14**, 1903 (2014).

[22] S. J. Pennycook and D. E. Jesson, High-Resolution Incoherent Imaging of Crystals, Phys. Rev. Lett. **64**, 938 (1990).

[23] C. L. Zheng and J. Etheridge, Measurement of chromatic aberration in STEM and SCEM by coherent convergent beam electron diffraction, Ultramicroscopy **125**, 49 (2013).

[24] N. Wahlberg, And A.Ø. madsen, implications of X-ray thermal diffuse scattering in integrated bragg intensities of silicon and cubic boron nitride, J. Appl. Crystallogr. **50**, 1791 (2017).

[25] R. Ishikawa, S. J. Pennycook, A. R. Lupini, S. D. Findlay, N. Shibata, and Y. Ikuhara, Single atom visibility in STEM optical depth sectioning, Appl. Phys. Lett. **109**, 163102 (2016).

[26] A. Y. Borisevich, A. R. Lupini, and S. J. Pennycook, Depth sectioning with the aberration-corrected scanning transmission electron microscope, Proc. Natl. Acad. Sci. **103**, 3044 (2006).

[27] R. F. Egerton, *Electron Energy-Loss Spectroscopy in the Electron Microscope* (Plenum Press, New York, 1996).

[28] E. C. Cosgriff and P. D. Nellist, A Bloch wave analysis of optical sectioning in aberration-corrected STEM, Ultramicroscopy **107**, 626 (2007).

[29] M. Mukai, E. Okunishi, M. Ashino, K. Omoto, T. Fukuda, A. Ikeda, K. Somehara, T. Kaneyama, T. Saitoh, T. Hirayama, and Y. Ikuhara, Development of a monochromator for aberration-corrected scanning transmission electron microscopy, Microscopy **64**, 151 (2015).

[30] O. L. Krivanek, T. C. Lovejoy, N. Dellby, T. Aoki, R. W. Carpenter, P. Rez, E. Soignard, J. Zhu, P. E. Batson, M. J. Lagos, R. F. Egerton, and P. A. Crozier, Vibrational spectroscopy in the electron microscope, Nature **514**, 209 (2014).

[31] T. Taniguchi and K. Watanabe, Synthesis of high-purity boron nitride single crystals under high pressure by using Ba–BN solvent, J. Cryst. Growth **303**, 525 (2007).

[32] T. Taniguchi, T. Teraji, S. Koizumi, K. Watanabe, and S. Yamaoka, Appearance of *n*-type semiconducting properties of *c*BN single crystals grown at high pressure, Jpn. J. Appl. Phys **41**, 109 (2002).